The strength of a constrained lithium layer

J.C. Stallard[1,2], S. Vema[1,2,3], C.P. Grey[2,3], V.S. Deshpande[1,2], N.A. Fleck[1,2,*]

[1] Department of Engineering, University of Cambridge, Trumpington St., Cambridge, CB2 1PZ, UK.
[2] The Faraday Institution, Quad One, Harwell Campus, Didcot, OX11 0RA, UK.
[3] Department of Chemistry, University of Cambridge, Lensfield Rd., Cambridge, CB2 1EW, UK.
*Corresponding Author. Email: naf1@eng.cam.ac.uk, Tel: +44 (0) 1223 7 48240.

Abstract

A constrained compression test is developed to replicate the mechanical state of a lithium filament within a solid state battery. Lithium microspheres are compressed between parallel quartz plates into a pancake shape of thickness on the order of 15 µm. Full adhesion with no slip exists between the lithium and platens, and the attendant mechanical constraint implies that the average pressure on the pancake-shaped specimens increases with increasing aspect ratio of radius to height. In addition to mechanical constraint, a thickness-dependent size effect is observed whereby the apparent flow strength of the lithium increases from 0.7 MPa in the bulk to 2.0 MPa at a thickness of 15 µm. The lithium deforms in a power-law creeping manner at room temperature, and to simplify interpretation of the results, the relative velocity of the loading platens is adjusted to ensure that the true compressive strain rate is held fixed at 10^{-3} s^{-1}. Additional measurements of lithium flow strength are obtained by subjecting the pancake-shaped specimens to simple shear. The size effect under shear loading is comparable to that in constrained compression. The observed size effect for lithium is consistent with that reported in the literature for lithium in indentation tests and in single pillar compression tests. Finally, the size effect of lithium in the power law creep regime is compared with that for rate-independent plasticity (for copper).

Keywords:

Li-ion battery, lithium filament, size effect, strain gradient plasticity, creep.

1. Introduction

Lithium-based solid-state batteries (SSBs) are under active development to meet the increasing global demand for electric vehicles (EVs) and for other battery powered devices such as electronic goods. The challenge is to increase battery capacity, power, reliability and life, but all at reduced cost. Solid electrolytes possess the desirable features of high ionic conductivity, low electronic conductivity, and high resistance to corrosion and combustion in contrast to liquid electrolytes [1]. However, the development of SSBs has been hampered by the formation of thin lithium filaments (sometimes termed 'dendrites') that crack the ceramic electrolyte and short-circuit the battery cells [2]. The cracks are commonly of opening 0.3 µm to 50 µm [3-5], and are internally filled (fully or partially) by as-plated lithium [3,4,6]. Both theoretical models and recent experiments [7] suggest that the normal compressive tractions on the lithium filaments is on the order of 100 MPa. Tractions of this magnitude far exceed the yield strength of bulk lithium, which is on the order of 1 MPa [8-10]. Thus, there is a need to measure the compressive strength of a thin lithium layer sandwiched between ceramic substrates which resembles the geometry of a lithium filament. It is conjectured that the Li layer can support a large compressive stress by a combination of mechanical constraint and a size effect (whereby Li in a thin film has a higher strength compared to bulk Li). The aim of the present study is to measure the relative magnitude of each contribution.

The existence of size effects in rate independent plasticity is now well-established from a wide range of tests on the micron and nanometre scales [11-13]. Strain gradient plasticity theories have emerged to explain the size effect at the micron scale [14,15]. In this regime, the strengthening with diminishing specimen size is linked to the presence of geometrically necessary dislocations; these dislocations are generated when a crystal is subjected to a plastic slip gradient in a direction other than that normal to the slip plane [11,16,17], and their density increases with decreasing specimen size. Geometrically necessary dislocations are additional

2

to statistically stored dislocations that accrue with slip. The macroscopic flow strength depends upon the total dislocation density, and the immediate consequence is the existence of a size effect: 'smaller is stronger'.

A size effect may persist when the length scale of a specimen or structure is reduced to a sub-micron level. For example, when a micropillar is compressed, dislocation nucleation sources are limited, and after a dislocation has nucleated it is strongly attracted to the free surface and is thereby annihilated [18,19]. Again, the observation is 'smaller is stronger'. But there is no reason that the functional dependence of strength upon size is preserved when new deformation mechanisms come into play.

Size effects have also been observed at an elevated temperature when deformation is by dislocation creep or by diffusional flow. Recall that the homologous temperature of a crystalline solid is defined by the ratio T/T_m, where T is absolute temperature in units of Kelvin and T_m is the melting temperature (also in Kelvin). At a sufficiently high homologous temperature, above about 0.4, the dominant mechanism switches from dislocation-mediated glide plasticity to power law creep or diffusional flow [20,21]. Size effects in the diffusional flow regime tend to be 'smaller is weaker' by the following argument. The diffusion of vacancies is driven by the spatial gradient of chemical potential; thus, the smaller is the size of sample, the greater is the gradient of their chemical potential and the faster is the macroscopic creep rate by diffusional flow [22-24].

There is currently limited understanding of size effects in the power law creep regime, but size effects are anticipated when the specimen size is comparable to the dislocation cell size of a bulk specimen; it is again expected that 'smaller is stronger'. Hot hardness tests on a range of metallic alloys support this reasoning [25-27]. For example, indium has a melting temperature of 157°C and a homologous temperature of 0.69 at room temperature.

3

Consequently, it undergoes power law creep at room temperature. Tagarielli and co-workers [28] have observed a size effect in indium for both bending and indentation loading, and invoked a strain gradient theory (Fleck and Hutchinson, 1997 [29]) to infer a material length scale of 100 μm which is approximately two orders of magnitude greater than that observed for rate independent plasticity in a range of metals and alloys.

The homologous temperature of lithium at room temperature is 0.65 [8], which is close to that for indium, and consequently bulk Li samples deform by power law creep at room temperature for strain rates in the range of 10^{-8} s^{-1} to 0.5 s^{-1} [8-10]. Experiments reveal that the room temperature hardness of lithium increases with diminishing indent size on the micron scale [9], and the compressive strength of micropillars increases with diminishing pillar diameter [30,31]. The purpose of the present study is to determine whether a size effect persists for a lithium layer of micron-scale thickness and sandwiched between two ceramic substrates. Two new test protocols are introduced in order to explore the size effect: the shear of a thin layer, inspired from the recent studies of Meng and co-workers [32,33] and the constrained compression of a thin layer, as analysed by Niordson and Hutchinson [34] for a rate independent solid.

There is a paucity of data on the creep response of lithium at the meso-scale (on a length scale between millimetres and microns. Sedlatschek et al [35] have measured the in-plane tensile response of a lithium foil of thickness 750 μm. This commercial foil was made by extrusion and hot rolling, and consequently it is highly textured. In-plane tensile tests reveals that the foil is isotropic in-plane but has a greater preference for yielding in the through thickness direction than in-plane. This is supported by the observation that in-plane axial tension results in a much larger strain in the through-thickness direction than in the width direction. Such a texture differs from that of as-plated lithium from a solid state electrolyte. The lithium specimens of the present study are made by a casting route and also do not possess

4

a pronounced deformation texture. The purpose of the present study is different from that of Sedlatschek et al [35]. In the present investigation, strain gradients are imposed on circular pancake-shaped specimens in either axial compression or in simple shear. In both types of test the dominant strain gradient is the variation of shear strain through the thickness of the specimen.

1.1 Scope of study

A test method is developed for the compression of a thin pancake-shaped layer of lithium sandwiched between quartz plates. The Li layer is subjected to a fixed value of compressive strain rate, and the effect of layer radius and thickness upon average pressure is determined. The state of slip versus no-slip between lithium and platens is explored by direct observation of the interface through the transparent platens. The flow strength of the lithium is estimated by an axisymmetric, constrained plasticity analysis of a thin layer between sticking platens. Shear tests are also performed on thin sandwich layers of Li to determine whether the size effect persists for shear loading. Finally, the observed size effects for lithium in the present study are compared with those reported in the literature for other types of test on lithium, and are also compared with the size-dependent, rate-independent plastic response of copper at room temperature.

2. Test protocol

2.1 Tensile tests on bulk lithium

Tensile tests were performed on dogbone samples from the same source of lithium and prepared by a closely related manufacturing route to that for the constrained compression and

shear tests of the present study. Samples for tensile testing were prepared inside an argon-filled glovebox (M.Braun Inertgas-systeme, Germany), in which the concentrations of water and oxygen were both maintained at below 0.1 ppm. Dogbone specimens of thickness 0.75 mm were cast by melting lithium foil (Fisher Scientific, UK) upon the surface of a 0.5 mm thick niobium sheet (Goodfellow Cambridge, UK) at a temperature of 190°C. Niobium was chosen because it is inert to molten lithium [36]. A flat surface for casting was obtained by adhering the niobium sheet to a steel substrate (using Loctite 270, Henkel, USA) and by levelling of the niobium sheet with the aid of a digital inclinometer (MW580-01, Moore & Wright, UK). The dogbone samples of width 6 mm and gauge length 25 mm were cut from the cast layer using a polypropylene punch, were peeled from the niobium substrate with titanium tweezers (3.TA.0, Ideal-Tek, Switzerland) and were thereby transferred to the grips of a screw-driven test machine (5944 test machine with 2 kN load cell, Instron, UK). Tensile tests were performed at a true strain rate of $\dot{\varepsilon} = 10^{-3}$ s^{-1} by suitable control of the grip velocity during each test. The axial strain in the samples was measured by laser tracking two reference markers adhered at each end of the sample gauge length.

2.2 Constrained compression tests

Constrained compression tests were performed on spherical droplets of lithium of diameter in the range 284 μm to 860 μm between quartz platens. The droplets were formed by melting small cut pieces of lithium foil on a non-reactive tantalum crucible (Kurt J. Lesker, UK) at a temperature of 200°C by manipulation with titanium tweezers, as illustrated in Fig. 1. Solidification occurred by air cooling, and the samples were removed from the tantalum crucible with the titanium tweezers. The grain size of the cast lithium samples was determined by mounting a cast lithium sphere in phenolic resin (Conducto-mount, Metprep, UK) and then

grinding with successively finer grades of silicon carbide paper (Metprep, UK) to produce a planar cross-section. Paraffin was used to cover the sample surface, to protect it from the air atmosphere, and to act as a lubricant during polishing. The polished cross-section was etched for 10 s with methanol [37], followed by rinsing with paraffin, and then examined in an optical microscope (020.520.007 DM/LP, Leica Microsystems, Germany) through the paraffin layer.

The apparatus used to conduct constrained compression tests is sketched in Fig. 2, and its use is explained as follows. Lithium spherical samples were compressed between two fused quartz optical flats which acted as loading platens. Each quartz flat (UQG Optics, UK) was of thickness 6 mm and diameter 25 mm. The lower quartz platen was clamped in a stainless steel holder, and a central hole in the holder allowed for continuous observation of the sample during compression with a digital microscope camera (Dino-Lite AM7115MZTL, GT Vision, UK). Fused quartz is resistant to chemical attack by lithium at room temperature but adheres strongly to the lithium [36]. Sufficient optical contrast between the lithium metal and upper steel holder was obtained by first darkening the holder by heat tinting it in air at 640°C. The upper platen was bonded to its stainless steel holder by contact adhesive (Loctite cyanoacrylate, Henkel, USA).

The lower platen holder was fastened to an aluminium frame by three screws, and the aluminium frame was bolted to the bed of the mechanical test machine. The gap between the upper and lower platens was measured at three equally spaced locations around the circumference of the platen by a capacitance technique, as follows. Pairs of opposing circular gold spots, of diameter 4 mm, were sputter-coated onto each quartz platen at a radial distance of 8 mm from the centre. Each opposing pair of spots behaved as the plates of a capacitor; the capacitance was sensed and logged using a capacitance transducer and accompanying software (FDC1004EVM board and software, Texas Instruments, USA).

The procedure for performing the compression tests was as follows. First, prior to insertion of the lithium sample, the three capacitors were used to align the quartz platens to be parallel to within 2 µm. To achieve this, the inclination of the lower platen was adjusted via the three screws that secured the lower platen holder to the aluminium frame. The lithium sample was then placed between the parallel platens, and its compressive response was measured at a fixed true strain rate of $\dot{\varepsilon} = 10^{-3}$ s^{-1}.

A clip gauge was used to measure the thickness of the sample and to maintain the strain rate by suitable control of the crosshead displacement. The capacitance of the three gold spots was also recorded throughout the experiment to confirm that the platens remained parallel. The cross-sectional area of the sample was measured throughout the test via the optical microscope that was positioned beneath the lower platen. After the specimen had been sufficiently compressed to be pancake in shape its volume was calculated from the product of the sample area and its measured height; it was confirmed that its volume remained constant during each test.

2.3 Shear tests on lithium films

The shear strength of a lithium film was determined as a function of film thickness by the following protocol. Pancake-shaped specimens of lithium and adhered quartz platens were manufactured by compressing spherical droplets of lithium to a desired thickness of 24 µm to 196 µm, and radius a of 2.2 mm to 3.7 mm. The lithium and quartz platens were removed from the compression rig, and were repositioned in the shear rig sketched in Fig. 3(a). The shear stress versus strain response of the lithium layer was determined by loading the upper edge of the lower quartz platen with a lubricated flat-tipped punch; paraffin was placed around the edge of the platens to minimise friction between the platens should they touch.

The load-line was aligned through the centre of the specimen and was inclined at $\theta = 25.6°$ to the vertical, see Fig. 3(a). This gave rise to small compressive stresses in addition to the shear stress, thereby reducing the likelihood of peeling during the shear tests. However, the magnitude of the normal load on the layer is much less than the compressive collapse load of the layer due to the large plastic constraint in compression. In all cases, the imposed shear strain rate was $\dot{\gamma} = \sqrt{3} \times 10^{-3}$ s^{-1}; consequently, the samples were subjected to the same value of von Mises effective plastic strain rate as that imposed in the tensile tests. The shear stress was determined by resolving the measured load along the shear direction of the lithium sample, see Fig. 3(b).

3. Results

A representative optical image of the etched microstructure is given in Fig. 4(a). The grain size was in the range $50 - 200$ µm.

3.1 Tensile tests on bulk lithium

The true stress versus true strain response at a strain rate of 10^{-3} s^{-1} is shown in Fig. 4(b) and reveals negligible strain hardening. This is consistent with the fact that the lithium deforms by power law creep at room temperature. Recall from the literature [9] that the power law creep exponent m equals 6.55 for bulk lithium [9], such that the uniaxial strain rate $\dot{\varepsilon}$ scales with the uniaxial stress σ according to

$$\frac{\dot{\varepsilon}}{\dot{\varepsilon}_0} = \left(\frac{\sigma}{\sigma_0}\right)^m \tag{1}$$

where the reference strain rate is chosen to be $\dot{\varepsilon}_0 = 10^{-3}$ s^{-1}. The flow strength σ_0 equals 0.72 MPa, as inferred from the mean measured true stress at the strain rate of 10^{-3} s^{-1} and uniaxial

logarithmic tensile strain $\varepsilon = 0.02$. The value $\sigma_0 = 0.72$ MPa of creep flow stress is in good agreement with the value of $0.68 - 0.85$ MPa reported in the literature [9,10]. The fracture surface imaged with a scanning electron microscope (LS-15 EVO, Carl Zeiss, UK) is shown in Fig. 4(c). In tension the lithium necks to a narrow chisel edge of micron-thickness; this is typical for a pure, soft and ductile metal.

3.2 Compression tests on constrained lithium film

Observation of state of stick/slip at interface

In order to interpret the compressive response of the sandwich specimens it is first necessary to determine the stick/slip condition at the interface between the lithium and the quartz platens. This is achievable due to the ability to observe the lithium/quartz interface through the transparent quartz platens. Digital Image Correlation (DIC) was used to analyse the images of a lithium sample during compression, and thereby to deduce the magnitude of sliding displacement between specimen and quartz platen. Representative images of the surface of the lithium at the start and two subsequent stages during a compression test are given in Fig. 5.

A typical result for the magnitude of interfacial slip is given in Fig. 5(c); it contains a plot of the jump in tangential displacement of the surface of the lithium between the images of Figs. 5(a) and (b). The tracked area is contained within the red circles in Figs. 5(a) and (b). Computational analysis[1] of the displacement field over intermediate frames between those reproduced in Figs. 5(a) and (b) confirm that the point-wise displacement is much less than the

---

[1] Digital image correlation and tracking functions for Matlab software (Mathworks, UK), maintained by Christoph Eberl. Accessed 2022.

change in the sample diameter. We conclude that the lithium fully adheres to the platens without slip during the compression test.

The projected area A of the sample during compression was measured from the images of contact area obtained with the digital microscope. The effective radius and height of the sample a and h are given by $a = \sqrt{A/\pi}$, and $h = V/A$, where V is the volume of the specimen[2]. The effective radius a and load F are both plotted as a function of specimen height h in Fig. 6(a) for a representative sample: both a and F increase sharply with decreasing height h. Write the aspect ratio of the sample as a/h, and the average pressure as $\bar{p} = F/A$, where F is the compressive load on the sample. Then, upon making use of the data of Fig. 6(a), the average pressure is plotted as a function of aspect ratio in Fig. 6(b); $\bar{p}$ increases with increasing aspect ratio in an almost linear fashion. The values of $(a, h, F, \bar{p})$ that correspond to the images of Figs. 5(a) and (b) are marked on the plots of Fig. 6 for illustration.

Average pressure as a function of aspect ratio and thickness of layer

The average pressure $\bar{p}$ is plotted as a function of aspect ratio a/h in Fig. 7(a), for spheres of initial diameter D from 284 µm to 860 µm . For all choices of sphere diameter, the average pressure $\bar{p}$ increases with increasing aspect ratio, and for specimens of the smallest diameter it exceeds 100 MPa. Further, note that, for any given value of aspect ratio, the average pressure increases with decreasing initial sample diameter and this implies the existence of a size effect.

---

[2] The volume V of the sample was determined as follows. The final sample thickness was measured at the end of experiment from the capacitance between the gold patches on each of the platens after unloading. This procedure was chosen to eliminate the elastic deformation of the platens when the specimen is under load. Multiplication of this thickness by the area determined from the images of the sample gives its volume V.

In order to separate the size effect from the role of plastic constraint, it is necessary to perform a plasticity analysis of the compressed film, and to deduce the dependence of the apparent flow strength of the lithium upon layer thickness. The details are given in a subsequent section.

3.3 Shear response of lithium sandwich layer

The measured shear stress τ is plotted as a function of engineering shear strain γ in Fig. 7(b). Define τ_Y as the peak shear stress of the measured response; then, the corresponding von Mises effective stress is $\sigma_Y = \sqrt{3}\tau_Y$. Recall that the imposed von Mises strain rate in the shear test is $\dot{\varepsilon} = 10^{-3}$ s^{-1}, then, the flow strength σ_0 is obtained via (1) as $\sigma_0 = \sigma_Y$. The flow strength σ_0 increases from 1.0 MPa to 1.3 MPa as the layer thickness is reduced from 200 μm to 24 μm. These values are slightly above the tensile strength of 0.72 MPa as reported in Fig. 4.

3.4 Interpretation of compression response of constrained layer to quantify the size effect

It remains to deduce the apparent flow strength of the lithium from the constrained compression tests. Full sticking between the lithium layer and quartz platens leads to an average compressive traction that much exceeds the creep flow strength σ_0. We proceed to make use of classical 'friction hill' theory to relate the average pressure $\bar{p}$ to the flow strength σ_0 of the lithium. Cheung and Cebon [38] have obtained an approximate analytic expression for the mean forging pressure $\bar{p}$ on a circular disc of radius a and height h for a power law creeping solid that satisfies (1); their expression reads

$$\frac{\bar{p}}{\sigma_0}\left(\frac{h\dot{\varepsilon}_0}{h}\right)^{1/m} = \left(\frac{m}{3m+1}\right)\left(\frac{m+2}{2}\right)^{1/m}\left(\frac{2a}{\sqrt{3}h}\right)^{(m+1)/m} \tag{2}$$

We shall make use of this expression to deduce the dependence of σ_0 upon h, and thereby

determine the degree of size effect in the constrained compression tests. But before we do so,

we first need to demonstrate that this expression is accurate at large m, as Cheung and Cebon

[38] only demonstrated agreement between prediction and finite element simulations for the

choice $m = 2.3$.

A comparison of (2) with finite element predictions using the commercial finite element

software ABAQUS[3] is given in Fig. 8 for the choice $m = 6.55$. In the finite element

simulations the lithium was idealised by an elastic-power law creeping solid, with a Young's

modulus of $E = 7.85$ GPa, a Poisson ratio of 0.38 [10], and with sticking friction between

lithium and rigid platens. A series of simulations were performed with a/h in the range of 0.1

to 100, and a mesh convergence study revealed that accurate results were obtained using 100

4-noded quadrilateral elements of type CAX4 through the half-thickness of lithium layer. Each

small strain simulation was performed at a fixed $\dot{h}$ and was continued until the axial forging

force became constant; typically, this required a reduction in thickness of layer Δh such that

$E\Delta h/a\sigma_0 > 2$. It is clear from Fig. 8 that for $m = 6.55$ the analytical expression (2) is

sufficiently accurate in comparison to the finite element simulations that it can be used to

deduce the dependence of σ_0 upon h in the constrained compression experiments.

An additional set of finite strain finite element simulations was performed in order to

determine the degree of deformation of a sphere that is required in order for its compressive

response between sticking platens to be adequately represented by the friction hill solution for

a circular cylinder. A series of finite element simulations were performed, and the build-up of

errors due to element distortion was addressed by periodic interruption of the loading and

---

[3] ABAQUS CAE (2020), supplied by Dassault Systèmes Simulia Corp., Cambridge, UK.

remeshing of the deformed configuration. The response for the sphere is included in Fig. 8 and reveals that the cylinder approximation is adequate for $a/h > 10$.

The data of Fig. 7(a) are replotted in Fig. 7(c) by making use of (2) to deduce the representative creep strength σ_0 as a function of thickness h. A trend emerges, such that σ_0 increases by a factor of approximately two from 1 MPa to 2 MPa as the height h is reduced from 600 μm to 15 μm.

The degree of size effect in the shear tests are compared in Fig. 7(c) with that observed in the compression tests. For both shear tests and compression tests, σ_0 is plotted as a function of the thickness of the lithium layer h. The deduced value of flow strength σ_0 in both types of test increase with decreasing thickness. A detailed analysis of size effects in both tests must await a rate analysis of strain gradient plasticity that builds upon the rate independent case of Niordson and Hutchinson [34].

3.5 Shear strength and tensile strength of the bond between lithium and quartz

Photographs of a representative lithium sample ($D = 2.14$ mm) between the quartz plates before and after shear testing are given in Figs. 9(a) and (b), respectively. There is no indication of slip at the interface between the quartz and the lithium, implying that the shear strength of the interface exceeds that of the lithium. We conclude that the measured shear stress τ is limited by shear yield of the lithium.

The high strength of the bonding between lithium and quartz in the compression testing was confirmed by performing a tensile test on the sandwiched lithium layer immediately after a compression test had been performed, see Fig. 9(c). The specimen was derived from a spherical droplet of diameter $D = 284$ μm and its height h at the end of the compression test

was 15 μm. The imposed tensile strain rate was 10^{-3} s^{-1} and the peak tensile strength was 6.0 MPa, which is much less that the average pressure of 109 MPa on the layer at the end of the compression tests. Edge peeling occurs with crack advance by microvoid coalescence. The fracture surface of the lithium has been imaged with a scanning electron microscope, and reveals that microvoids are spaced on the order of one to three times the layer thickness (15 μm). Occasionally, debonding occurs such that the underlying quartz is observed. This failure mode and level of tensile strength is suggestive of cavitation whereby voids can grow without limit from vanishingly small initial defects [39,40].

4. Discussion

We proceed to consider the current results on size effects of lithium in the context of the existing literature on size effects of lithium from indentation [9] and micro-pillar compression studies [30,31] at room temperature. To do so, the flow strength of lithium is plotted as a function of characteristic specimen dimension L in Fig. 10(a) by making use of the data of the present study and that in the literature. The relevant length scale in the compression of micropillars or whiskers is their diameter, whereas in a sandwich specimen under compression or shear it is the layer height (with data taken from the present study). For the indentation tests the relevant specimen length scale is defined as $L = \sqrt{A}$, where A is the projected area of the indent, see Appendix A for details. We note in passing that the compressive strength of the micro-pillar tests by Xu et al [31] lies at the top of the scatter band in Fig. 9(a). This may be due to strengthening of the Li by alloying with Ga, as Xu et al [31] used Ga for FIB cutting of their specimens.

In order to account for the effect of rate dependence, the flow strengths are reported for tests performed at a strain rate of 10^{-3} s^{-1} where possible. If this is not achievable, then the

measured strength is scaled by a suitable factor based on power law creep: the factor equals the ratio of strain rate of 10^{-3} s^{-1} to that in the experiment, raised to the power of $1/m$, where the power law creep exponent is $m = 6.55$ [9]. The hardness data of Fincher et al (2020) is converted to flow strength by assuming that the ratio of indentation pressure to flow strength equals three, as explained by Tabor [41] and as analysed by Bower et al [42] in the context of power law creep. For these data, no adjustment for loading rate was performed.

Note from Fig. 10(a) that the data from a wide range of tests gives an overall trend of 'smaller is stronger'. The length scale spans 4 orders of magnitude and the observed flow strength spans slightly more than 2 orders of magnitude. The mechanisms of plastic flow over this wide range of length scale varies from the collective behaviour of dislocation cells at the larger lengths to the nucleation of individual dislocations, such as prismatic punching beneath an indenter at the smaller lengths [17].

The literature on size effects in plasticity has focussed on rate independent dislocation glide that occurs at room temperature in metallic alloys of high melting temperature. For illustration, the dependence of flow strength of copper upon structural length scale L has been assembled from the literature in Appendix A. The broad envelope of the data plotted in Fig. A1 for copper and in Fig. 10(a) for lithium are replotted in Fig. 10(b) in the form of σ_0/E, versus L/b where E is the Young's modulus (at room temperature) and b is the magnitude of the Burger's vector. For copper, σ_0 denotes the yield strength σ_Y in Fig. 10(b). Here, we assume that for lithium and copper, respectively, E equals 7.82 GPa [10] and 124 GPa [43], and b equals 0.304 nm [8], and 0.250 nm [44]. Remarkably, the strengths of the rate independent copper and the rate dependent lithium overlap in the range $200 < l/b < 10^4$. At larger structural dimension, $l/b > 10^4$, the normalised strength of lithium is an order of magnitude lower than that of copper and this is attributed to thermal activation of creep processes.

Predictions of the ideal tensile strength σ_{Max} of a body centred cubic (B.C.C.) crystal such as lithium [20,45] and a face centred cubic crystal (F.C.C.), such as copper [20,46] are included in Fig. 9(b). The maximum predicted shear stress of each lattice τ_{Max} is related to an equivalent tensile stress σ_{Max} according to $\sigma_{Max} = \sqrt{3}\tau_{Max}$. At the lowest normalised length scales $l/b = 200$ for which data presently exists, the greatest measured strength of lithium and copper both lie approximately a factor of 2 below the ideal strengths of their respective lattices.

5. Concluding remarks

The constrained compression test and shear test are complementary means of assessing a size effect in lithium: the height of a compression specimen varies during the test, and strain gradients necessarily arise as a result of the sticking nature of the platens. In contrast, the strain state in the shear test, with sticking platens, can be uniform or non-uniform. The constrained compression test has the additional merit that it attempts to reproduce the mechanical state of lithium within a filament in a solid electrolyte.

The present study provides direct evidence that a sandwiched lithium layer can support large compressive tractions due to the plastic constraint associated with sticking between the lithium and quartz substrate. Similar constraint effects arise when lithium is plated out from a solid state electrolyte to form a filament. This high constraint prevents the lithium from being extruded out along the length of the filament towards a free surface of the plated electrode. In addition to the plastic constraint, an additional size effect is present whereby a thin layer of lithium behaves in a stronger manner than a thick layer. It is conjectured that this size effect is associated with the presence of a spatial gradient in plastic strain.

The masterplot of Fig. 10(b) reveals that size effects in the power law creep regime resemble those in rate independent plasticity, albeit by comparing the response of lithium and

copper. There is a need to generate such a plot for the same solid over a wide temperature regime to confirm the validity of this finding.

Acknowledgements

References

[1] M. Weiss, R. Ruess, J. Kanatscheew, Y. Levartovsky, N.R. Levy, P. Minnmann, L. Stolz, T. Waldmann, M. Wolfhart-Mehrens, D. Aurbach, M. Winter, Y. Ein-Eli, J. Janek, Fast charging of lithium-ion batteries: a review of materials aspects, Adv. Eng. Mater. 11 (33) (2021) 2101126.

[2] K. Kerman, A. Luntz, V. Viswanathan, Y.M. Chiang, Z. Chen, Review—Practical challenges hindering the development of solid state li ion batteries, J. Electrochem. Soc. 164 (7) (2017) A1731-A1744.

[3] Z. Ning, D.S. Spencer Jolly, G. Li, R. De Meyere, S.D. Pu, Y. Chen, J. Kasemchainan, J. Ihli, G. Gong, B. Liu, D.L.R. Melvin, A. Bonnin, O. Magdysyuk, P. Adamson, G.O. Hartley, C.W. Munroe, T.J Marrow, P.G. Bruce, Visualizing plating-induced cracking in lithium-anode solid-electrolyte cells, Nat. Mater. 20 (8) (2021) 1121-1129.

[4] L. Porz, T. Swamy, B.W. Sheldon, D. Rettenwander, T. Frömling, H.L. Thaman, S. Berendts, R. Uecker, W.C. Carter, Y.M. Chiang, Mechanism of lithium metal penetration through inorganic solid electrolytes, Adv. Eng. Mater. 7 (20) (2017) 1701003.

[5] D.S. Jolly, Z. Ning, G.O. Hartley, B. Liu, D.L.R. Melvin, P. Adamson, J. Marrow, P.G. Bruce, Temperature dependence of lithium anode voiding in argyrodite solid-state batteries, ACS Appl. Mater. Interfaces 13 (19) (2021) 22708-22716.

[6] E. Kazyak, R. Garcia-Mendez, W.S. LePage, A. Sharafi, A.L. Davis, A. J. Sanchez, K.H. Chen, C. Haslam, J. Sakamoto, N.P. Dasgupta, Li penetration in ceramic solid electrolytes: operando microscopy analysis of morphology, propagation and reversibility, Matter 2 (4) (2020) 1025-1048.

[7] C.D. Fincher, C.E. Athanasiou, C. Gilgenbach, M. Wang, B.W. Sheldon, W.C. Carter, Y.M. Chiang, Controlling dendrite propagation in solid-state batteries with engineered stress, Joule 6 (12) (2022) 2794-2809.

[8] P.M. Sargent, M.F. Ashby, Deformation mechanism maps for alkali metals, Scripta Metall. 18 (2) (1984) 145-150.

[9] C.D. Fincher, D. Ojeda, Y. Zhang, G.M. Pharr, M. Pharr, Mechanical properties of metallic lithium: from nano to bulk scales, Acta Mater. 186 (2020) 215-222.

[10] A. Masias, N. Felten, R. Garcia-Mendez, J. Wolfenstine, J. Sakamoto, Elastic, plastic and creep mechanical properties of lithium metal, J. Mater. Sci. 54 (3) (2019) 2585-2600.

[11] N.A. Fleck, G.M. Muller, M.F. Ashby, J.W. Hutchinson, Strain gradient plasticity: theory and experiment, Acta Metall. Mater. 42 (2) (1994) 475-487.

[12] J.B. Pethica, R. Hutchings, W.C. Oliver, Hardness measurement at penetration depths as small as 20 nm, Philos. Mag. A 48 (4) (1983) 593-606.

[13] J.R. Greer, W.C. Oliver, W.D. Nix, Size dependence of mechanical properties of gold at the micron scale in the absence of strain gradients. Acta Mater. 53 (6) (2005) 1821-1830.

[14] W.D. Nix, Mechanical properties of thin films, Metall. Trans. A 20 (11) (1989) 2217-2245.

[15] J.Y. Shu, N.A. Fleck, E. Van der Giessen, A. Needleman, Boundary layers in constrained plastic flow: comparison of nonlocal and discrete dislocation plasticity, J. Mech. Phys. Solids 49 (6) (2001) 1361-1395.

[16] J.F. Nye, Some geometrical relations in dislocated crystals, Acta Metall. 1 (2) (1953) 153-162.

[17] M.F. Ashby, The deformation of plastically non-homogeneous materials, Philos. Mag. 21 (170) (1970) 399-424.

[18] J.R. Greer, W.D. Nix, Nanoscale gold pillars strengthened through dislocation starvation, Phys. Rev. B 73 (24) (2006) 245410.

[19] M.D. Uchic, D.M. Dimiduk, J.N. Florando, W.D. Nix, Sample dimensions influence strength and crystal plasticity, Science 305 (5686) (2004) 986-999.

[20] H.J. Frost, M.F. Ashby, Deformation-mechanism maps: the plasticity and creep of metals and ceramics, Permagon, Oxford, 1982.

[21] E. Artz, M.F. Ashby, R.A. Verrall, Interface controlled diffusional creep, Acta Metall. 31 (12) (1983) 1977-1989.

[22] K.S. Kumar, H. Van Swygenhoven, S. Suresh, Mechanical behavior of nanocrystalline metals and alloys, Acta Mater. 51 (19) (2003) 5743-5774.

[23] J. Schiøtz, K.W. Jacobsen, A maximum in the strength of nanocrystalline copper, Science 301 (5638) (2003) 1357-1359.

[24] D.G. Xie, R.R. Zhang, Z.Y. Nie, J. Li, E. Ma, J. Li, Z.W. Shan, Deformation mechanism maps for sub-micron sized aluminium, Acta Mater. 188 (2020) 570-578.

[25] O. Franke, J.C. Trenkle, C.A. Schuh, Temperature dependence of the indentation size effect, J. Mater. Res. 25 (7) (2010) 1255-1229.

[26] P.S. Phani, W.C. Oliver, A direct comparison of high temperature nanoindentation creep and uniaxial creep measurements for commercial purity aluminium, Acta Mater. 111 (2016) 31-38.

[27] J.M. Wheeler, C. Kirchlechner, J.S. Micha, J. Michler, D. Kiener, The effect of size on the strength of FCC metals at elevated temperatures: annealed copper, Philos. Mag. 96 (32-34) (2016) 3379-3395.

[28] S.P. Iliev, X. Chen, M.V. Pathan, V.L. Tagarielli. Measurements of the mechanical response if indium and of its size dependence in bending and indentation. Mater. Sci. Eng: A 683 (2017) 244-251.

[29] N.A. Fleck, J.W. Hutchinson. Strain gradient plasticity. Adv. Appl. Mech. 33 (C) (1997) 295-361.

[30] L. Zhang, T. Yang, C. Du, Q. Liu, Y. Tang, J. Zhao, B. Wang, T. Chen, Y. Sun, P. Jia, H. Li, L. Geng, J. Chen, H. Ye, Z. Wang, Y. Li, H. Sun, X. Li, Q. Dai, Y. Tang, Q. Peng, T. Shen, S. Zhang, T. Zhu, J. Huang, Lithium whisker growth and stress generation in an in situ atomic force microscope-environmental transmission electron microscope set-up, Nat. Nanotechnol. 15 (2) (2020) 94-98.

[31] C. Xu, Z. Ahmad, A. Aryanfar, V. Viswanathan, J.R. Greer, Enhanced strength and temperature dependence of mechanical properties of Li at small scales and its implications for Li metal anodes, Proc. Natl. Acad. Sci. U. S. A. 114 (1) (2017) 57-61.

[32] Y. Mu, J.W. Hutchinson, W.J. Meng, Micro-pillar measurements of plasticity in confined Cu thin films. Extrem. Mech. Lett. 1 (2014) 62-69.

[33] Y. Mu, X. Zhang, J.W. Hutchinson, W.J. Meng, Measuring critical stress for shear failure of interfacial regions in coating/interlayer/substrate systems through a micro-pillar testing protocol, J. Mater. Res. 32 (8) (2017) 1421-1431.

[34] C.F. Niordson, J.W. Hutchinson, Basic strain gradient plasticity theories with application to constrained film deformation, J. Mech. Mater. Struct. 6 (1-4) (2011) 395-416.

[35] T. Sedlatschek, J. Lian, W. Li, M. Jiang, T. Wierzbicki, M.Z. Bazant, J. Zhu. Large-deformation plasticity and fracture behavior of pure lithium under various stress states. Acta Mater. 208 (2021) 116730.

[36] D.W. Jeppson, J.L. Ballif, W.W. Yuan, B.E. Chou, Lithium literature review: lithium's properties and interactions, U.S.A., 1978.

[37] H.C. Nash, C.S. Smith, Single-crystal elastic constants of lithium, J. Phys. Chem. Solids 9 (2) (1959) 113-118.

[38] C.Y. Cheung, D. Cebon, Thin film deformation behaviour of power-law creeping materials, J. Eng. Mech. 123 (11) (1997) 1138-1152.

[39] M.F. Ashby, F.J. Blunt, M. Bannister. Flow characteristics of highly constrained metal wires. Acta Metall. 37 (7) (1989) 1847-1857.

[40] A.R. Akisanya, N.A. Fleck. Fatigue and creep of a constrained metal wire. Acta Metall. Et Mater. 41 (1) (1993) 121-131.

[41] D. Tabor, The hardness of metals, Clarendon Press, Oxford, 1951.

[42] A.F. Bower, N.A. Fleck, A. Needleman, N. Ogbonna, Indentation of a power law creeping solid, Proc. R. Soc. A 441 (1911) (1993) 97-124.

[43] M.F. Ashby, D.R.H. Jones, Engineering materials 1: an introduction to properties, application and design, Butterworth-Heinmann, Oxford, 2012.

[44] W.J. Poole, M.F. Ashby, N.A. Fleck, Micro-hardness of annealed and work-hardened copper polycrystals, Scr. Mater. 34 (4) (1996) 559-564.

[45] A. Kelly, Strong Solids, Clarendon Press, Oxford, 1966.

[46] W.R. Tyson, Theoretical strength of perfect crystals, Philos. Mag. 14 (131) (1966) 925-936.

[47] Y. Liu, A.H.W. Ngan, Depth dependence of hardness in copper single crystals measured by nanoindentation, Scr. Mater. 44 (2) (2001) 237-241.

[48] J.G. Swadener, E.P. George, G.M. Pharr, The correlation of the indentation size effect measured with indenters of various shapes, J. Mech. Phys. Solids 50 (4) (2002) 681-694.

[49] K.W. McElhaney, J.J. Vlassak, W.D. Nix, Determination of indenter tip geometry and indentation contact area for depth-sensing indentation experiments, J. Mater. Res. 13 (5) (1998) 1300-1306.

[50] S.N. Dub, Y.Y. Lim, M.M. Chaudhri. Nanohardness of high purity Cu (111) single crystals: the effect of indenter load and prior plastic sample strain. J. Appl. Phys. 107 (4) (2010) 043510.

[51] G. Feng, A.S. Budiman, W.D. Nix, N. Tamura, J.R. Patel, Indentation size effects in single crystal copper as revealed by synchrotron x-ray microdiffraction, J. Appl. Phys. 104 (4) (2008) 043501.

[52] Y.Y. Lim, M.M. Chaudhri, The effect of the indenter load on the nanohardness of ductile metals: an experimental study on polycrystalline work-hardened and annealed oxygen-free copper, Philos. Mag. A 79 (12) (1999) 2979-3000.

[53] K.K. McLaughlin, W.J. Clegg, Deformation underneath low-load indentations in copper, J. Phys. D: Appl. Phys. 41 (7) (2008) 074007.

[54] M. Rester, C. Motz, R. Pippan, Indentation across size scales - a survey of indentation-induced plastic zones in copper {111} single crystals, Scr. Mater. 59 (7) (2008) 742-745.

[55] D. Kiener, C. Motz, T. Schöberl, M. Jenko, G. Dehm, Determination of mechanical properties of copper at the micron scale, Adv. Eng. Mater. 8 (11) (2006) 1119-1125.

[56] D. Liu, Y. He, X. Tang, H. Ding, P. Hu, P. Cao, Size effects in the torsion analysis of microscale copper wires: experiment and analysis, Scr. Mater. 66 (6) (2012) 406-409.

[57] D. Liu, Y. He, D.J. Dunstan, B. Zhang, Zhipeng Gan, Peng Hu, H. Ding, P. Hu, P. Cao, Towards a further understanding of size effects in the torsion of thin metal wires: an experimental and theoretical assessment, Int. J. Plast. 41 (2013) 30-52.

[58] A.T. Jennings, J.R. Greer, Tensile deformation of electroplated copper nanopillars, Philos. Mag. 91 (7-9) (2011) 1108-1120.

[59] A.T. Jennings, M.J. Burek, J.R. Greer, Microstructure versus size: mechanical properties of electroplated single crystalline Cu nanopillars, Phys. Rev. Lett. 104 (13) (2010) 135503.

[60] A.T. Jennings, J. Li, J.R. Greer, Emergence of strain-rate sensitivity in Cu nanopillars: transition from dislocation multiplication to dislocation nucleation, Acta Mater. 59 (14) (2011) 5627-5637.

[61] X. Zhang, B. Zhang, Y. Mu, S. Shao, C.D. Wick, B.R. Ramachandran, W.J. Meng, Mechanical failure of metal/ceramic interfacial regions under shear loading, Acta Mater. 138 (2017) 224-236.

Appendix A. Size effects in copper

Size effects in rate independent glide plasticity are summarised for pure copper. Data has accumulated from tests [32,33,44,47-61] on specimens of dimension 100 nm to 100 μm, see Fig. A1. These tests include the indentation of both work-hardened and annealed copper [44,47-54], torsion and tension tests on annealed wires [11,56,57], compression and tensile tests on copper micropillars [55,58-60], and shear tests on thin layers of copper adhered to ceramic substrates [32,33,61]. For each experiment a measure of the von Mises effective flow strength σ_Y is deduced and plotted against a representative experiment dimension L, which intends to approximate the strength-controlling dimension of the volume within which yield processes occur. The measures of flow strength σ_Y and length L used here are illustrated in Fig. A1(a), and are defined as follows:

- ***Torsion of wires:*** The strength σ_Y is derived from torque Q and wire diameter D according to $\sigma_Y = 36Q/\left(\pi\sqrt{3}D^3\right)$. The strength is measured at a surface strain $\varepsilon = \kappa D/2\sqrt{3} = 0.01$ where κ is twist per unit length. Note that $\kappa D/2$ is the magnitude of engineering shear strain at the wire surface. The characteristic dimension is $L = D$.

- ***Tension of wires:*** σ_Y is the nominal tensile stress of a wire of diameter D measured at a strain of $\varepsilon = 0.01$. The characteristic dimension is $L = D$.

- ***Indentation of annealed and work-hardened copper:*** The Tabor relation $\sigma_Y = H/3$ is assumed, in which hardness $H = F/A$, F is the indentation load, and A is the projected indentation area. It is emphasised that almost all indentation studies included in Fig. A1 use direct measurements of the indentation area, obtained after the indentation tip has been withdrawn, and measured by optical, scanning electron or scanning-probe microscopy. The characteristic dimension is $L = \sqrt{A}$.

- ***Compression and tension of copper pillars:*** The dimension L is the specimen diameter, and σ_Y is the unixial flow strength.

- ***Shear strength tests:*** The von Mises effective stress is $\sigma_Y = \sqrt{3}\tau$, where τ is the peak shear strength of the copper layer. The dimension L is the layer thickness.

An overall trend of an increasing flow strength σ_Y with decreasing specimen dimension L is evident in Fig. A1, but the detailed scaling varies depending upon the value of characteristic dimension L, the experimental method, and the degree of work hardening in the test specimen. The trend of increasing strength σ_Y with decreasing L that exists for copper wires tested in torsion is absent for wires under tension; this is attributed to the presence of geometrically necessary dislocations that accompany strain gradients [11] when the wire is subjected to torsion. The flow strength measured in shear tests also lies above data measured in uniaxial tension and compression or indentation experiments. This effect may be due to the hard ceramic substrates restricting the motion of dislocations within the sample, and thereby inducing a gradient of plastic strain [15]. For this reason, the thickness of the layer may affect the flow strength in shear [15].

Figure captions

Fig. 1: (a) Sketch of the apparatus used to cast lithium spheres, (b) photograph of as-cast lithium spheres.

Fig. 2: The apparatus for lithium compression tests: (a) overview; and (b) sectional view through sample and platens showing positioning of clip gauge and capacitive thickness sensors.

Fig. 3: (a) Apparatus for shear test, and (b) specimen geometry.

Fig. 4: (a) Grain structure of an as-cast lithium sample, as imaged by optical microscopy. (b) The true stress-true strain response of cast lithium in tension. (c) Knife-edge neck of lithium fracture surface, obtained by a scanning electron microscope (SEM).

Fig. 5: Images of a lithium sample of initial diameter $D = 860$ μm viewed through a quartz platen with an optical microscope at an aspect ratio a/h of (a) 44.5 and (b) 86.7. (c) Contours of in-plane displacement magnitude by DIC.

Fig. 6: (a) Radius a of layer and load F plotted against thickness of layer h during compression at fixed true strain rate of $\dot{\varepsilon} = 10^{-3}$ s^{-1}, and (b) average pressure $\bar{p}$ versus aspect ratio a/h. The lithium sample initial diameter is $D = 860$ μm, for which images are presented in Fig. 5; the points in each graph correspond to images of Fig. 5(a) and (b).

Fig. 7: (a) Average pressure $\bar{p}$ versus aspect ratio a/h in compression tests of lithium spheres with selected initial diameter D. (b) Shear strength τ versus shear strain γ from shear tests of lithium layers of selected thickness h. (c) Inferred flow strength σ_0 from compression tests versus thickness h. The strength σ_0 from independent shear tests are included in (c).

Figure 8: Geometry of cylindrical layer investigated in finite element simulations, and effect of strain rate exponent m upon compressive response of a cylindrical layer. The predicted evolution of $\bar{p}$ and a/h for sphere compression is included.
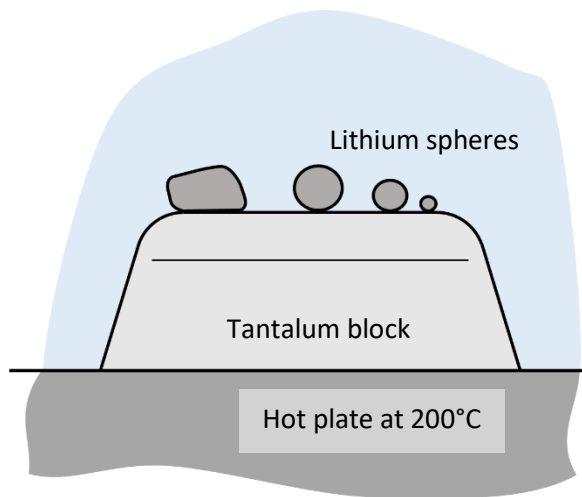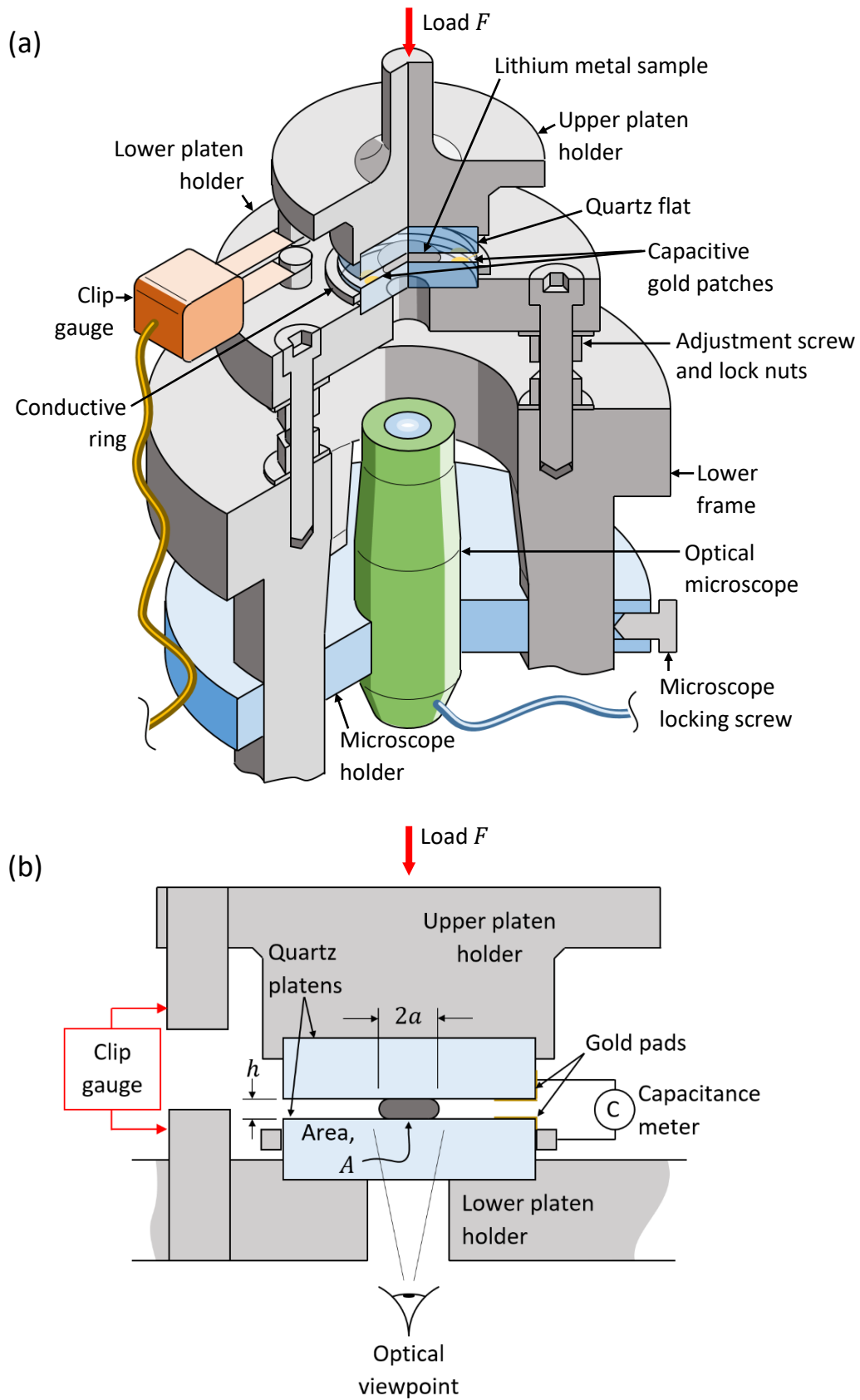
Fig. 9: Optical images of a shear test sample viewed through a quartz platen (a) before and (b) after a shear test. (c) Sketch of constrained tension test and fracture of the lithium layer, and (d) failure by cavitation of microvoids, observed in a scanning electron microscope.

Fig. 10: (a) Flow strength σ_0 of lithium versus characteristic dimension L taken from the present study and from the literature. Data of (a) are plotted in (b) alongside data for copper plotted in Fig. A1; σ_0 and L from the present study and from the literature are normalised by the Young's moduli E and Burgers vectors b of lithium and copper, respectively. For copper, σ_0 denotes the yield strength σ_Y.

Fig. A1: (a) The set of tests reported in the literature to deduce the yield strength σ_Y of copper. (b) Plot of σ_Y versus characteristic dimension L in the tests.

Figures

(a)

(b)

5 mm

Fig. 1: (a) Sketch of the apparatus used to cast lithium spheres, (b) photograph of as-cast lithium spheres.

Fig. 2: The apparatus for lithium compression tests: (a) overview; and (b) sectional view through sample and platens showing positioning of clip gauge and capacitive thickness sensors.
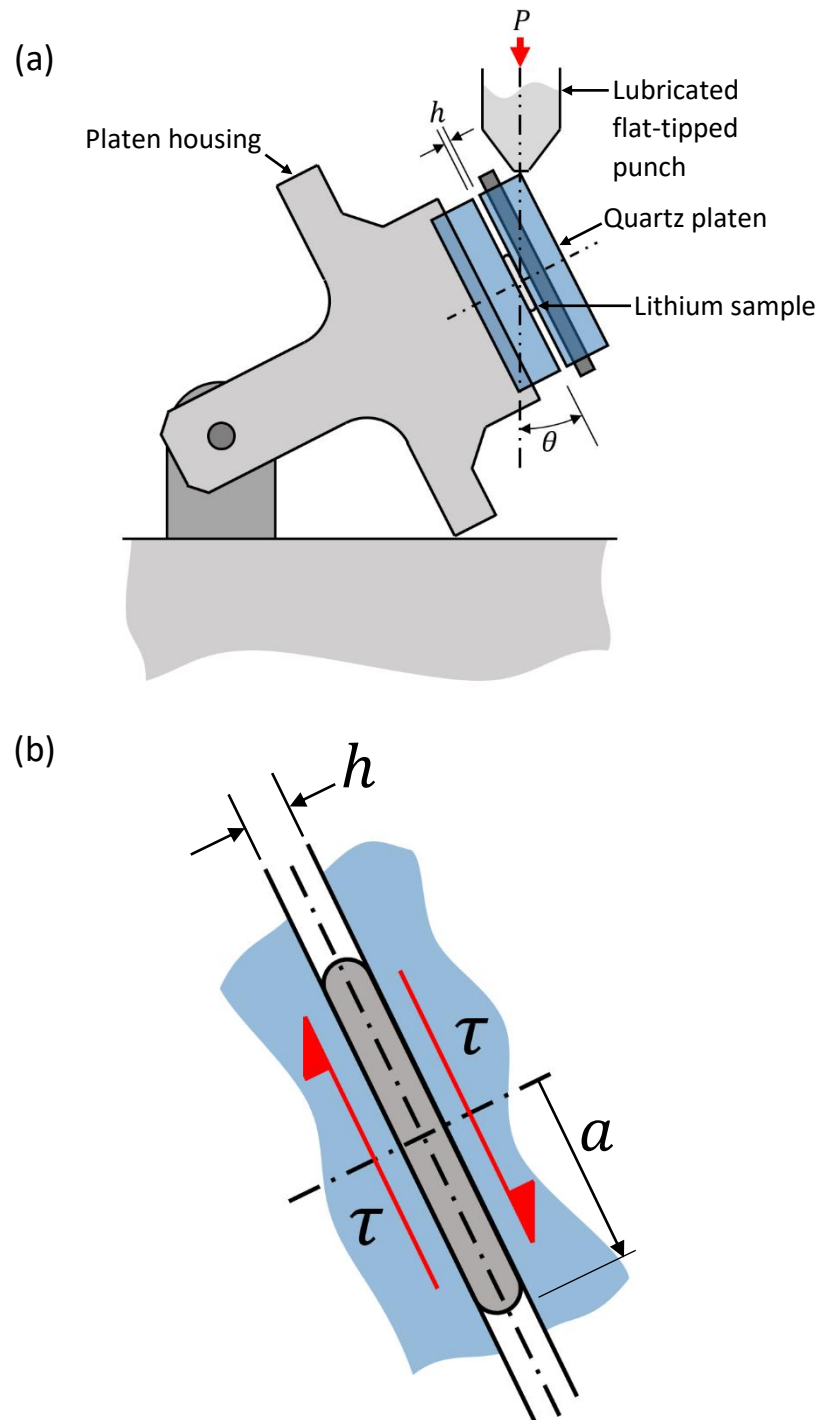
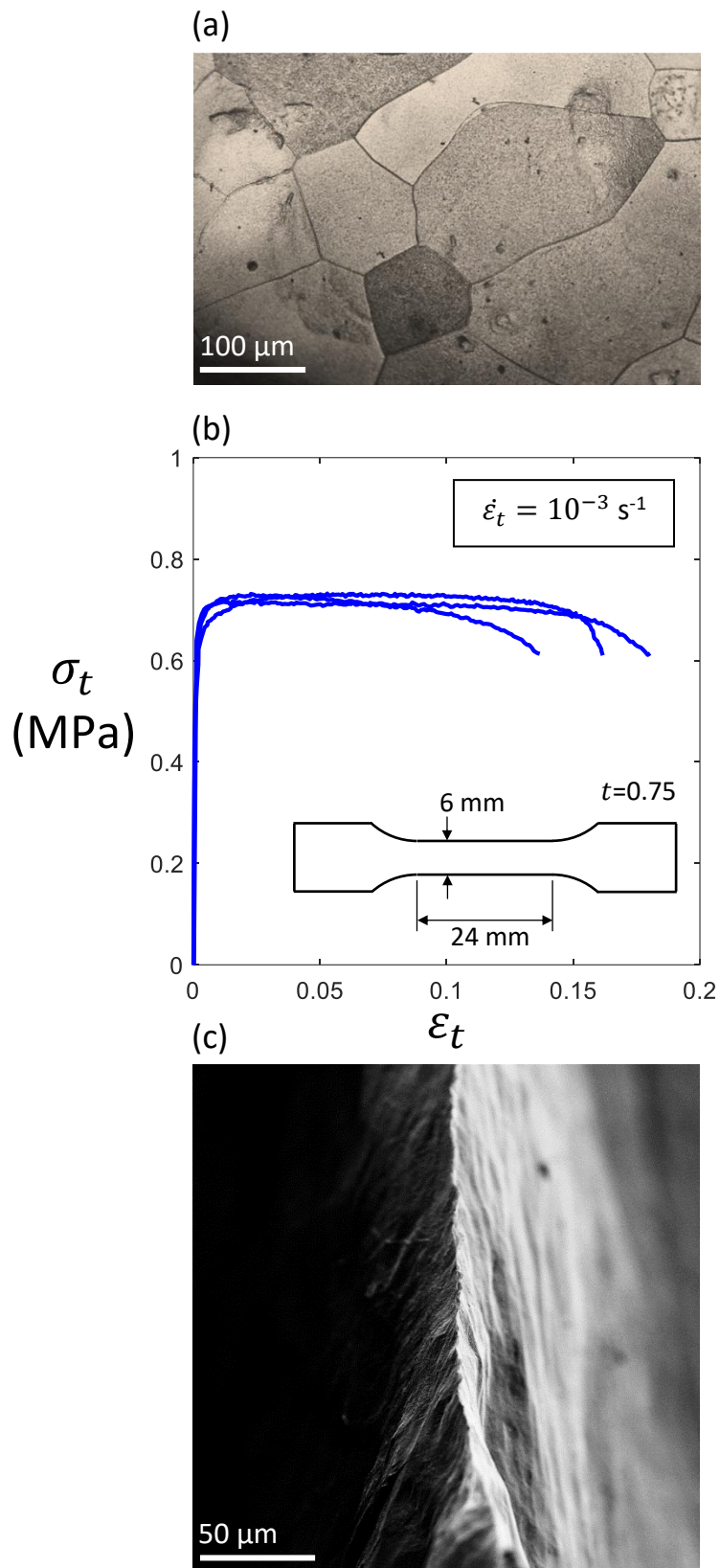Fig. 3: (a) Apparatus for shear test, and (b) specimen geometry.

(a)

100 µm

(b)

$\dot{\varepsilon}_t = 10^{-3}$ s⁻¹

σ_t (MPa)

6 mm

t=0.75

24 mm

ε_t

(c)

50 µm

Fig. 4: (a) Grain structure of an as-cast lithium sample, as imaged by optical microscopy. (b) The true stress-true strain response of cast lithium in tension. (c) Knife-edge neck of lithium fracture surface, obtained by a scanning electron microscope (SEM).
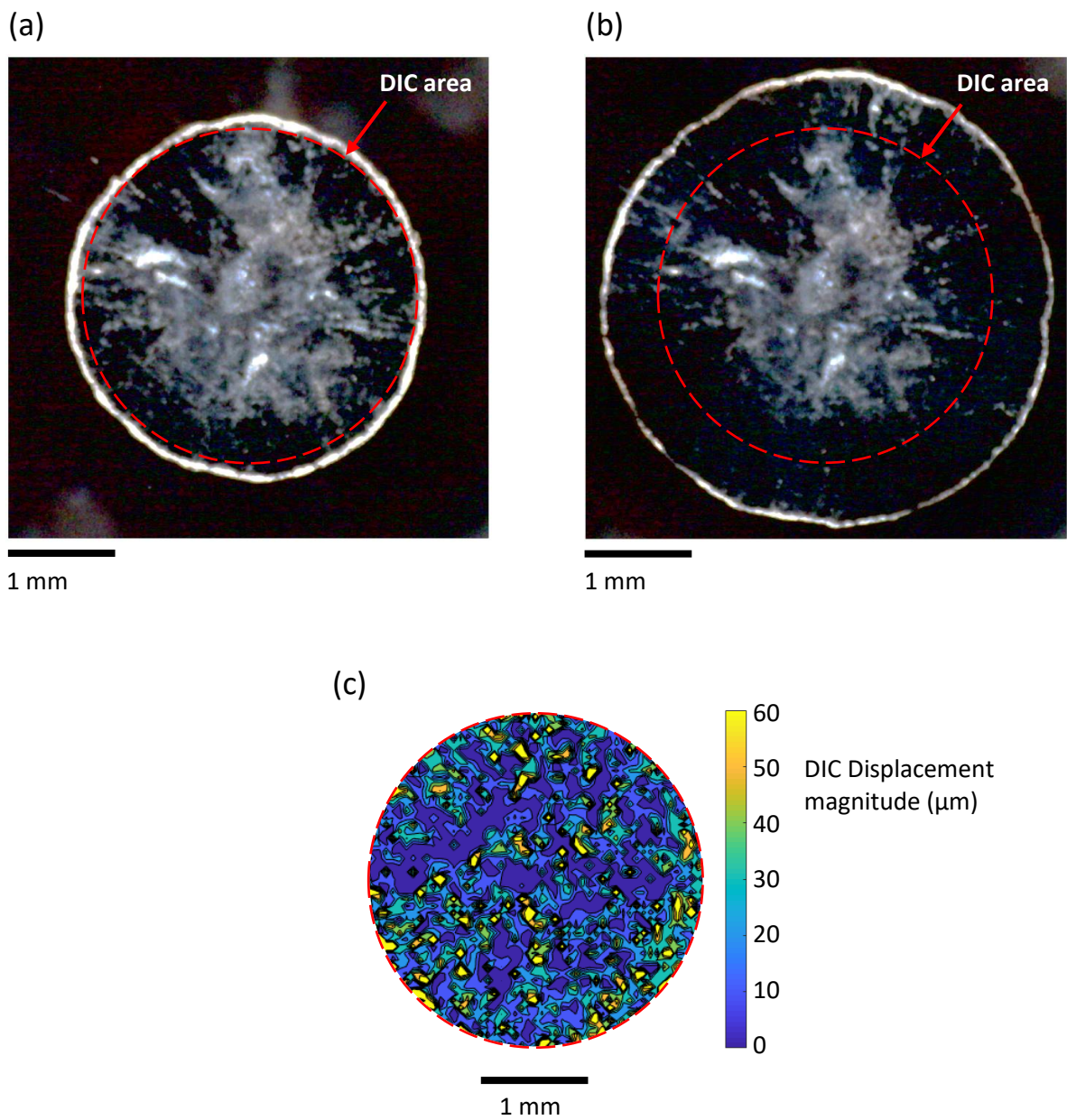
Fig. 5: Images of a lithium sample of initial diameter $D = 860$ µm viewed through a quartz platen with an optical microscope at an aspect ratio a/h of (a) 44.5 and (b) 86.7. (c) Contours of in-plane displacement magnitude by DIC.
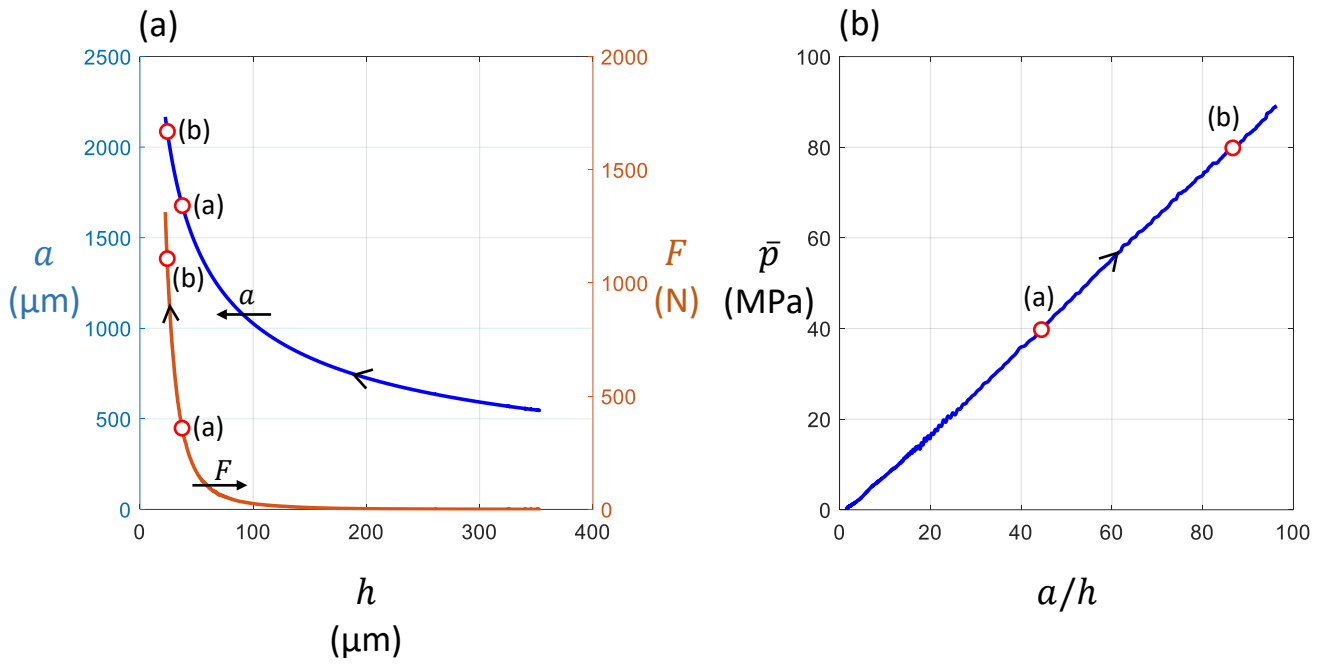
Fig. 6: (a) Radius a of layer and load F plotted against thickness of layer h during compression at fixed true strain rate of $\dot{\varepsilon} = 10^{-3}$ s^{-1}, and (b) average pressure $\bar{p}$ versus aspect ratio a/h. The lithium sample initial diameter is $D = 860$ µm, for which images are presented in Fig. 5; the points in each graph correspond to images of Fig. 5(a) and (b).
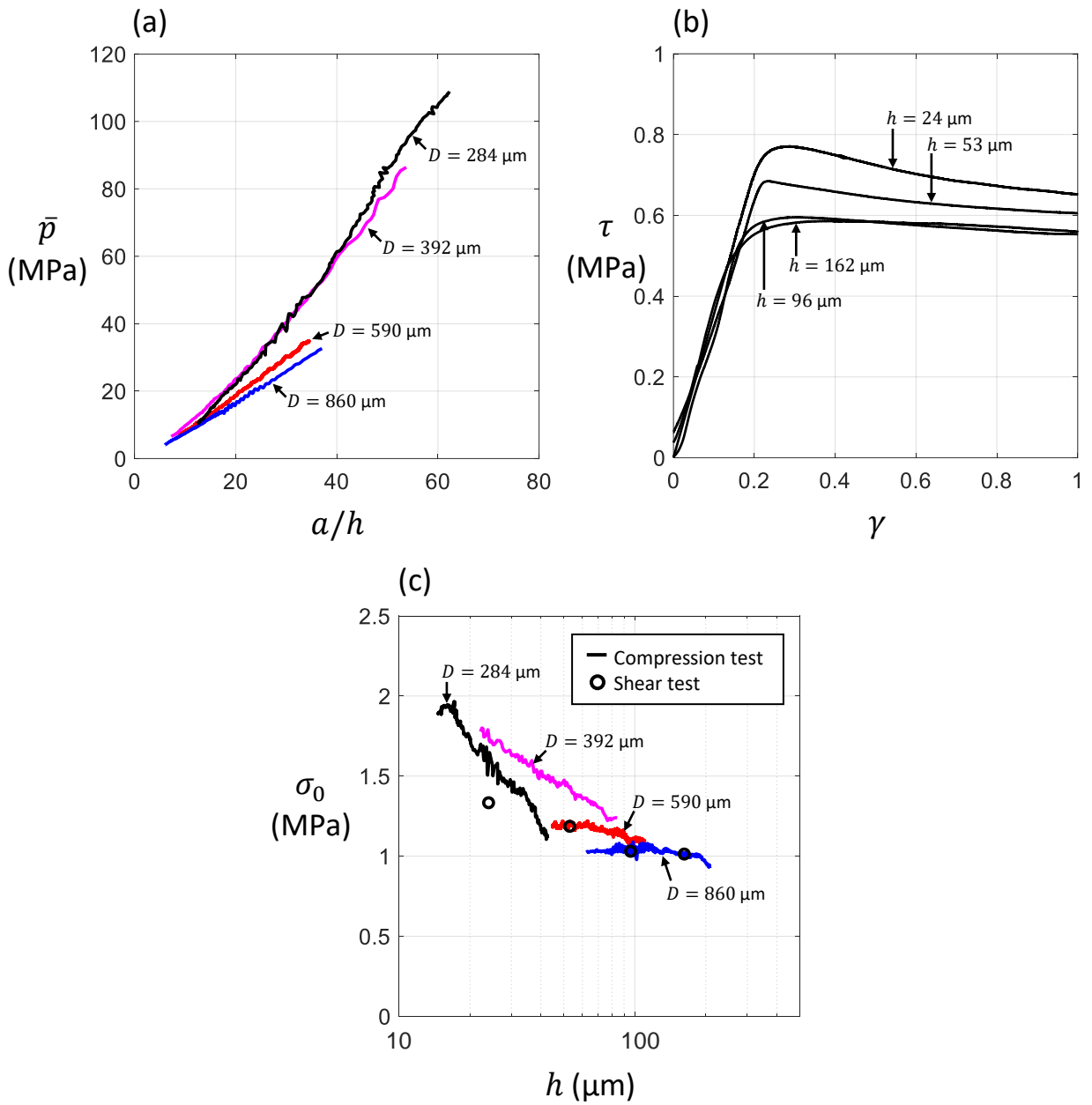
Fig. 7: (a) Average pressure $\bar{p}$ versus aspect ratio a/h in compression tests of lithium spheres with selected initial diameter D. (b) Shear strength τ versus shear strain γ from shear tests of lithium layers of selected thickness h. (c) Inferred flow strength σ_0 from compression tests versus thickness h. The strength σ_0 from independent shear tests are included in (c).
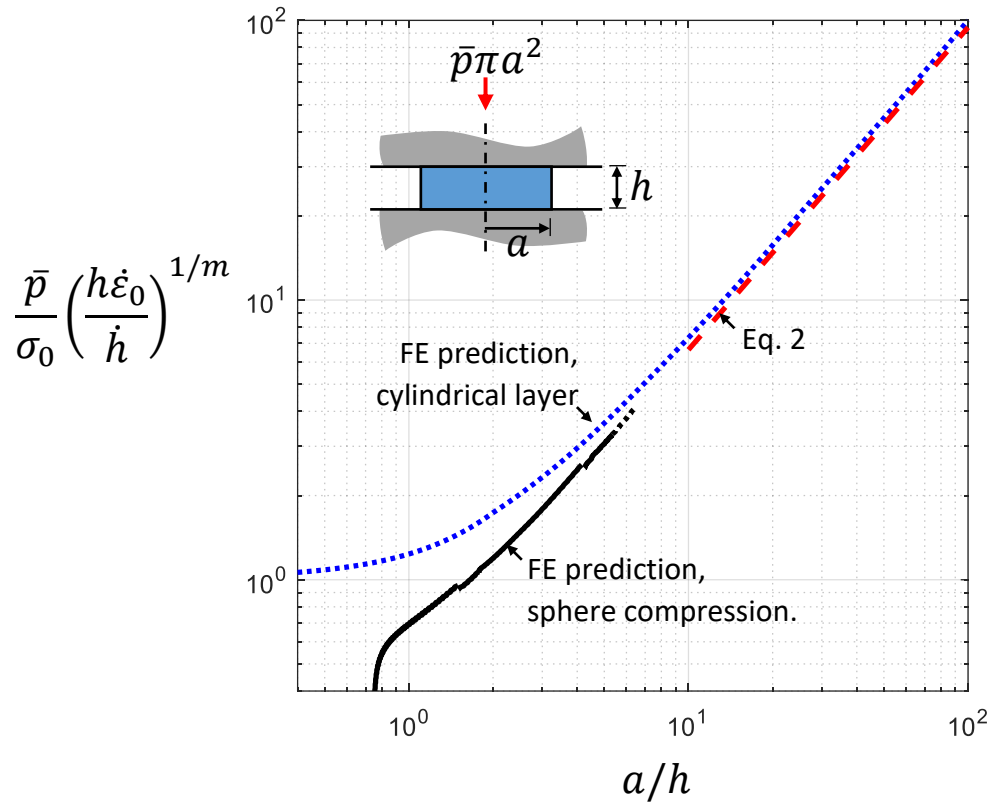
Figure 8: Geometry of cylindrical layer investigated in finite element simulations, and effect of strain rate exponent m upon compressive response of a cylindrical layer. The predicted evolution of $\bar{p}$ and a/h for sphere compression is included.

(a)

(b)

2 mm

(c)

Tension

Quartz
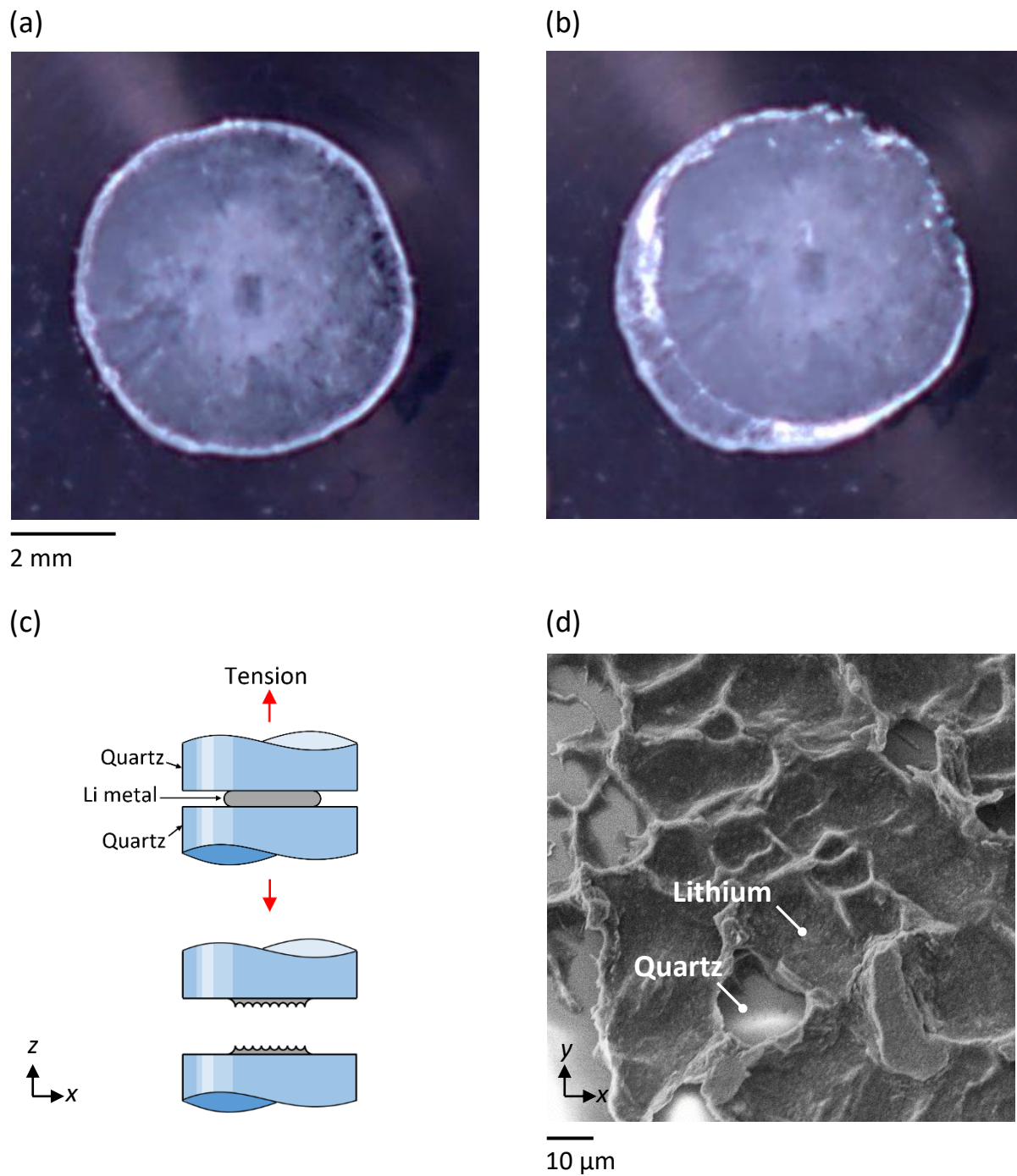Li metal
Quartz

z
x

(d)

Lithium
Quartz

y
x

10 μm

Fig. 9: Optical images of a shear test sample viewed through a quartz platen (a) before and (b) after a shear test. (c) Sketch of constrained tension test and fracture of the lithium layer, and (d) failure by cavitation of microvoids, observed in a scanning electron microscope.
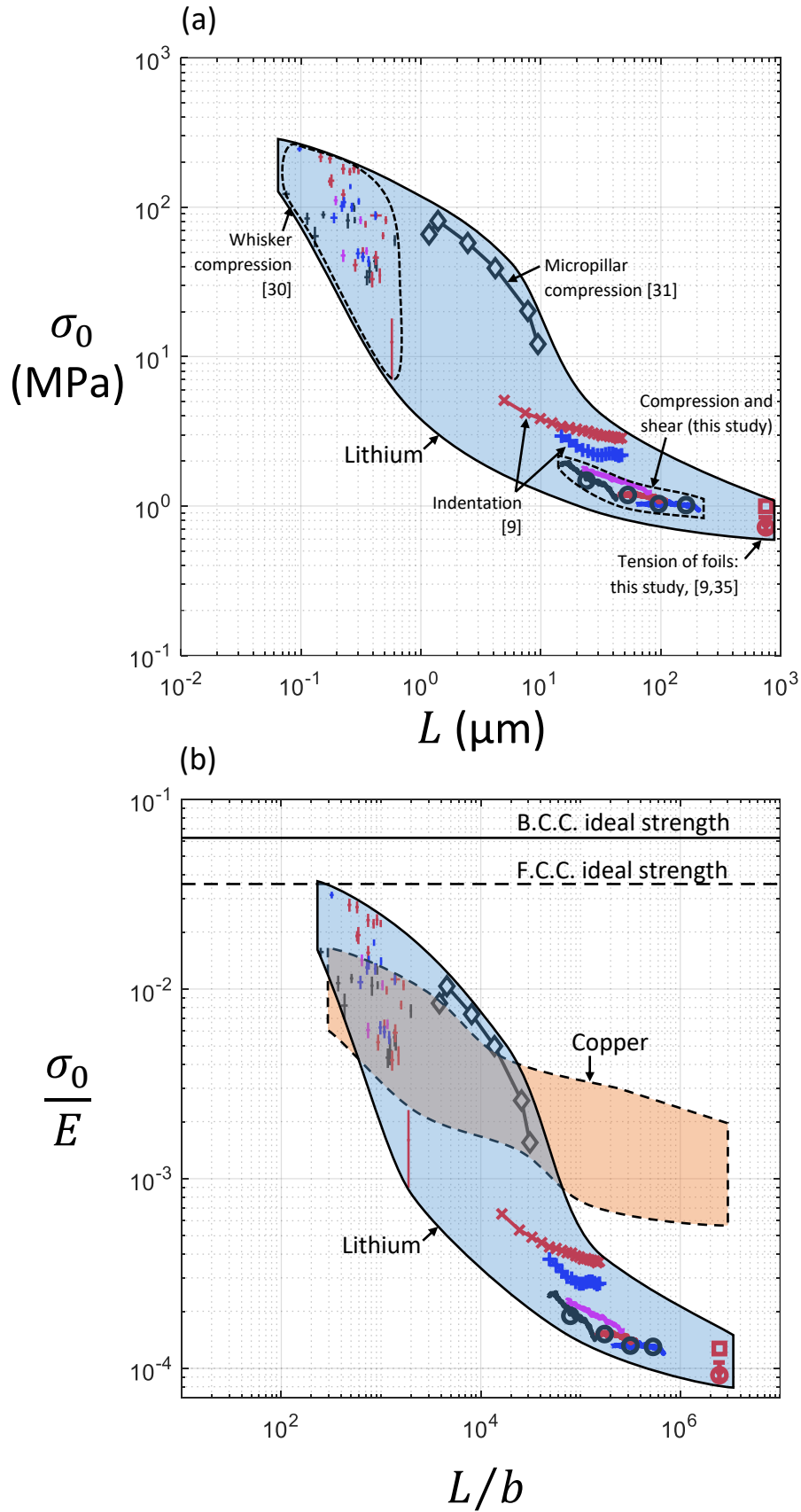
Fig. 10: (a) Flow strength σ_0 of lithium versus characteristic dimension L taken from the present study and from the literature. Data of (a) are plotted in (b) alongside data for copper plotted in Fig. A1; σ_0 and L from the present study and from the literature are normalised by the Young's moduli E and Burgers vectors b of lithium and copper, respectively. For copper, σ_0 denotes the yield strength σ_Y.

36

(a)

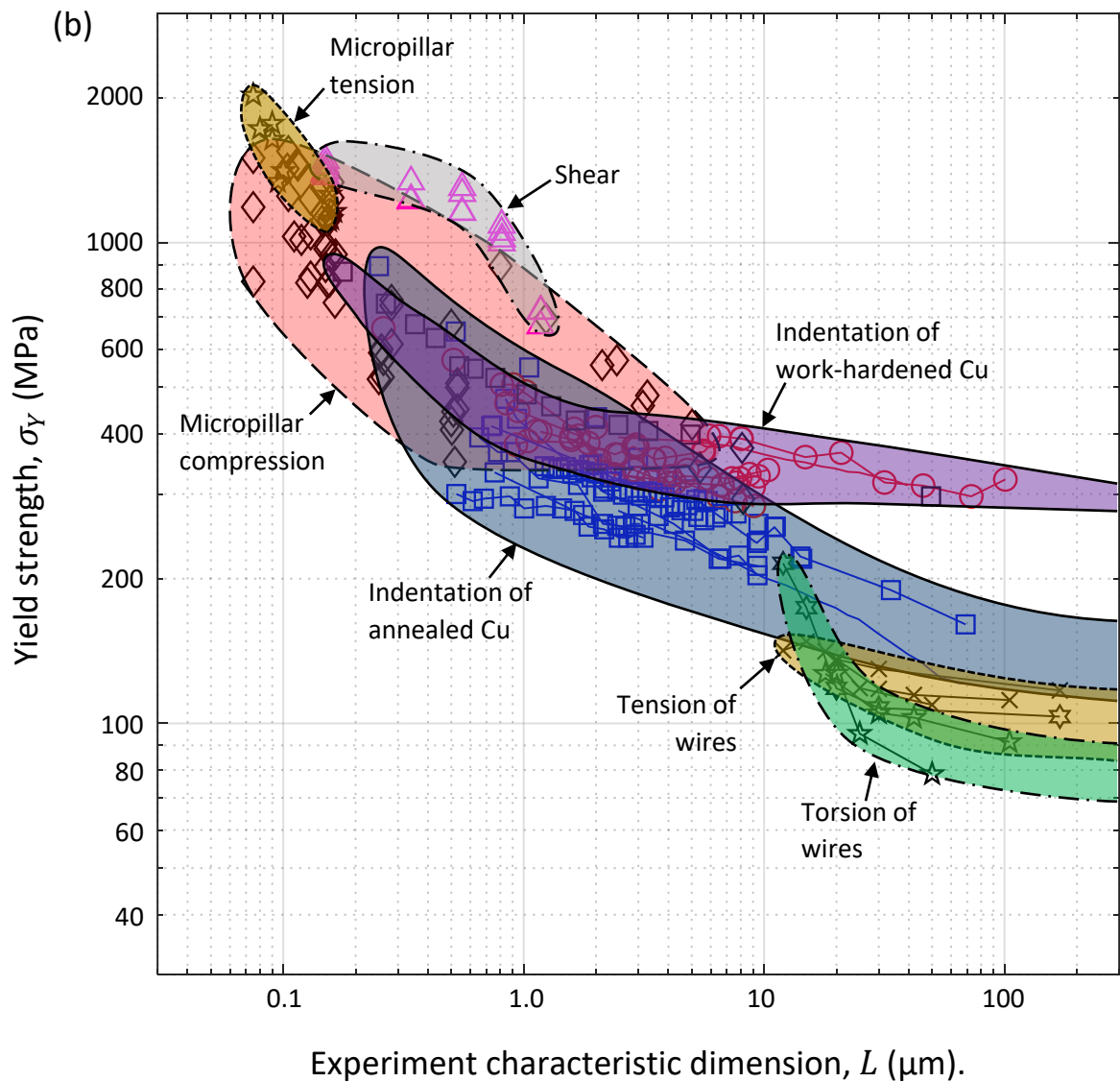| Test method	Micropillar tension	Shear tests	Micropillar compression	Berkovich indentation	Wire torsion	Wire tension
References	[58]	[32,33,61]	[55,58-60]	[44,47-54]	[11,56,57]	[11,56,57]
Characteristic dimension L / Representative strength σ	σ_Y, Slip plane, L, σ_Y	F, τ, τ, L, F, $\sigma_Y = \tau_Y\sqrt{3}$	σ_Y, L, σ_Y, Slip plane	F, Projected area, A, $L = \sqrt{A}$, $\sigma_Y = \dfrac{F}{3A}$	Torque Q, L, $\sigma_Y = \dfrac{12\sqrt{3}}{\pi}\dfrac{Q}{L^3}$	σ_Y, L, σ_Y

(b)

Fig. A1: (a) The set of tests reported in the literature to deduce the yield strength σ_Y of copper. (b) Plot of σ_Y versus characteristic dimension L in the tests.